Nanomechanical cutting of boron nitride nanotubes by atomic force microscopy

Nanomechanical cutting of boron nitride nanotubes by atomic force microscopy

Meng Zheng[1,6]**, Xiaoming Chen**[1,6]**, Cheol Park**[2,3]**, Catharine C Fay**[4]**, Nicola M Pugno**[5] **and Changhong Ke**[1]

[1] Department of Mechanical Engineering, State University of New York at Binghamton, Binghamton, NY 13902, USA
[2] National Institute of Aerospace, Hampton, VA 23666, USA
[3] Department of Mechanical and Aerospace Engineering, University of Virginia, Charlottesville, VA 22904, USA
[4] NASA Langley Research Center, Hampton, VA 23681, USA
[5] Department of Civil, Environmental and Mechanical Engineering, University of Trento, Trento, I-38123, Italy

E-mail: cke@binghamton.edu

Abstract
The length of nanotubes is a critical structural parameter for the design and manufacture of nanotube-based material systems and devices. High-precision length control of nanotubes by means of mechanical cutting using a scriber has not materialized due to the lack of the knowledge of the appropriate cutting conditions and the tube failure mechanism. In this paper, we present a quantitative nanomechanical study of the cutting of individual boron nitride nanotubes (BNNTs) using atomic force microscopy (AFM) probes. In our nanotube cutting measurements, a nanotube standing still on a flat substrate was laterally scribed by an AFM tip. The tip–tube collision force deformed the tube, and eventually fractured the tube at the collision site by increasing the cutting load. The mechanical response of nanotubes during the tip–tube collision process and the roles of the scribing velocity and the frictional interaction on the tip–tube collision contact in cutting nanotubes were quantitatively investigated by cutting double-walled BNNTs of 2.26–4.28 nm in outer diameter. The fracture strength of BNNTs was also quantified based on the measured collision forces and their structural configurations using contact mechanics theories. Our analysis reports fracture strengths of 9.1–15.5 GPa for the tested BNNTs. The nanomechanical study presented in this paper demonstrates that the AFM-based nanomechanical cutting technique not only enables effective control of the length of nanotubes with high precision, but is also promising as a new nanomechanical testing technique for characterizing the mechanical properties of tubular nanostructures.

(Some figures may appear in colour only in the online journal)

1. Introduction

One dimensional (1D) tubular nanostructures (i.e., nanotubes), which possess unique structural and physical properties, have been actively investigated for a number of engineering applications, such as nanodevices, sensors and composites. The length of nanotubes is a critical structural parameter for the design and manufacture of nanotube-based material systems and devices [1]. For instance, the lengths of nanotubes directly impact their natural frequencies for resonator applications and their electric resistances for electronics applications. The tube length can be controlled in the synthesis stage by tuning the chemical reaction conditions and controlling the tube growth rate and time [2, 3]. However, it is difficult to achieve a nanometer-level precision in controlling the tube length using this approach because it is extremely

---

[6] These two authors contributed equally to this work.

challenging, if not impossible, to have precise control of the nanotube growth rate as well as the start and/or the end of chemical synthesis processes [4]. Several post-synthesis approaches have also been proposed to control the tube length by cutting nanotubes. Mechanical milling/grinding [5–7], microtoming [8], ultrasonication [9–12], as well as chemical etching methods using acids [13–19] have been reported to cut and shorten carbon nanotubes (CNTs) in either dry or aqueous conditions. However, the cutting of tubes using these methods occurs randomly and in the entire batch with little-to-no control of the cutting position and the tube length at an individual tube level. Furthermore, chemical etching also inevitably introduces structural defects and/or surface contaminations to the shortened nanotubes. High-precision cutting of individual nanotubes was reported using electron beams inside electron microscopes [20–23]. Scanning probe microscopy, a versatile nanoscale imaging and manipulation technique, was also adopted to cut individual nanotubes. Most notably, Venema *et al* reported cutting single-walled CNTs using a positively biased scanning tunneling microscopy tip [24], while similar work was reported by Kim *et al* of cutting individual multi-walled CNTs using a negatively biased atomic force microscopy (AFM) tip [25]. The nanotube cutting mechanisms in both studies were attributed to the disruption of nanotube lattices by current-induced electric etching; its effectiveness in shortening CNTs with a nanometer resolution was demonstrated. However, such techniques essentially require conductive substrates in order to pass a current through the tube. Therefore, they may not work for electrically insulating substrates (e.g. SiO_2) that are widely used for CNT-based nanoelectronics and/or electrically insulating nanotubes. Alternatively, AFM probes with sharp tips are promising as mechanical scribing tools to engineer substantial local radial deformations in nanotubes [26, 27] and/or cut individual nanotubes remaining on substrates. Scribing is a simple machining technique and is commonly used in our daily life. By sliding a scriber on the surface of a target material, scratches are made as a result of both the normal and the shear forces exerted by the scriber. Similarly, it is expected that a nanotube remaining on a flat substrate can be cut by using a nano-scriber. Even though AFM has been widely used in the manipulation of nanotubes [27–29], high-precision length control of nanotubes by means of mechanical cutting using AFM-based nano-scribing techniques has not been investigated, and little is known about the appropriate cutting conditions and the tube failure mechanism. In this paper, we investigate the nanomechanical cutting of individual boron nitride nanotubes (BNNTs) using AFM-based nano-scribing techniques. This work capitalizes on the recent advances in studying the radial deformability of BNNTs using AFM [30–34], and focuses on investigating the nanomechanical cutting conditions and the tube failure mechanisms.

BNNTs are a light-weight and highly crystalline tubular nanostructure, and are composed of partially ionic and hexagonal B–N bonding networks [35, 36]. BNNTs not only have a similar structure to CNTs, but also possess many extraordinary physical properties that are comparable

to or even superior to those of CNTs. For example, a Young's modulus of up to 1.3 TPa and a tensile strength of up to 33 GPa have been reported for BNNTs [37–41]. Recent studies show that BNNTs possess much higher shear strength than CNTs [42]. The thermal conductivity of BNNTs reportedly exceeds 3000 W m^{-1} K^{-1} [43, 44]. Unlike the metallic or semiconductive properties of CNTs, BNNTs possess large bandgaps of 5–6 eV [35, 36, 45, 46], which are largely independent of the tube chirality. BNNTs are also quite resistant to oxidation at high temperature in air [47] and inert to harsh chemicals [48]. Applications of BNNTs include mechanical and/or thermal reinforcing additives for polymeric and ceramic composites [49], protective shields/capsules [50], and electrical insulators and optoelectronics [51]. BNNTs were chosen as the tested tubes in this study due to their representative structural and mechanical properties. The experimental methodologies presented in this paper are completely general and can be applied directly to the study of nanomechanical cutting of other types of tubular nanostructures (e.g. CNTs).

Nanomechanical cutting of nanotubes using AFM is essentially a mechanical machining process, which is accompanied by collision-induced mechanical deformation of the nanotubes and the nanotube fracture phenomenon. Quantitative characterization of the cutting conditions not only helps in understanding the nanotube failure mechanism, but also creates a means to quantify the fracture strength of the nanotubes, both of which are of importance for a complete understanding of their structural and mechanical properties and in the pursuit of their engineering applications.

2. Results and discussion

2.1. AFM-based nanomechanical cutting scheme and nanotube fracture modes

Figure 1(a) illustrates our experimental scheme of cutting individual BNNTs lying on flat substrates by using AFM-based nano-scribing techniques. A sharp AFM probe is first engaged with the substrate with a specified compressive load and then controlled to move laterally and perpendicularly toward a nanotube. Once the AFM tip collides with the nanotube, the resulting collision force compresses the nanotube and may lead to substantial transverse deformation or even fracture of the nanotube at the collision site, as shown in the drawing. Fracture of the nanotube can be considered as a result of the maximum collision-induced stress in the tube reaching or exceeding its fracture strength. The collision force is contributed by the normal compression of the tube and the AFM tip as well as their tangential frictional interactions [34]. The tip–tube collision influences the normal and torsional deflections of the AFM cantilever. A laser reflection scheme is employed to measure the normal and torsional deflections of the AFM cantilever by recording the respective horizontal and vertical motions of the reflected laser spot on a quadratic photo-detector. From the measured deflections of the AFM cantilever, both the normal and the lateral forces applied to the AFM tip at the moment of collision with the nanotube
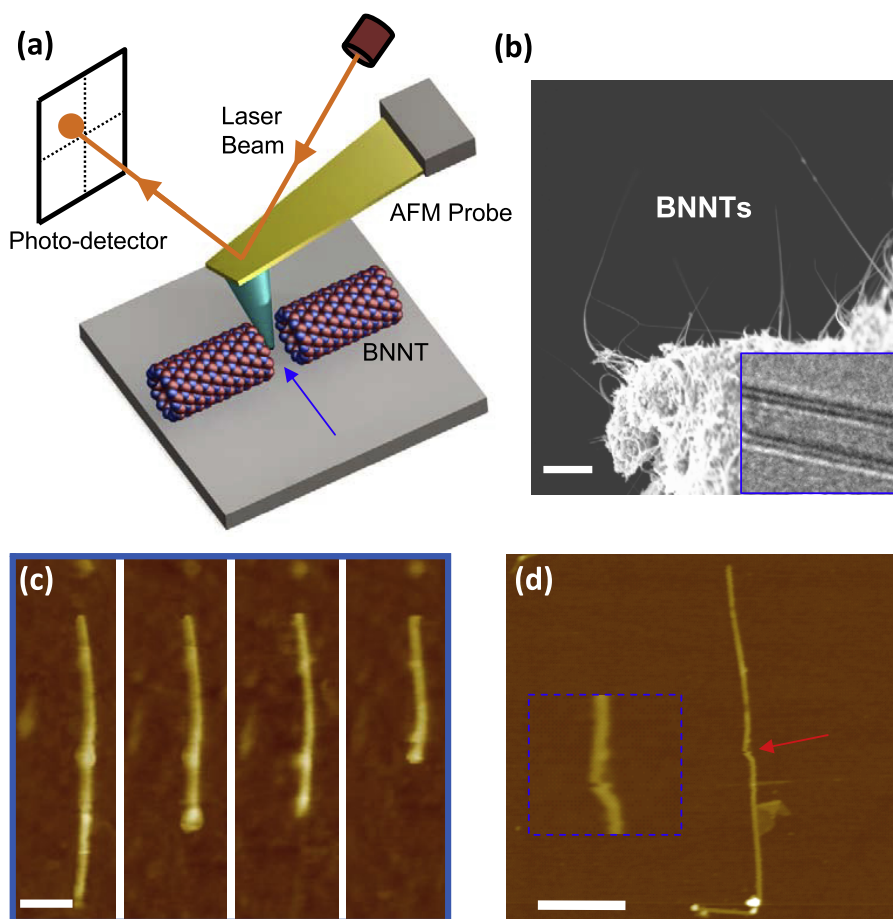
Figure 1. (a) Schematic illustration of nanomechanical cutting of a BNNT by lateral AFM. The blue arrow indicates the moving direction of the AFM tip. For simplicity, the drawing does not display the bending and stretching deformations of the tube at the cutting site. (b) SEM image of as-synthesized BNNTs using PVC methods. Inset: a representative HRTEM image of double-walled BNNTs with 2.9 nm outer diameter. (c) A series of AFM images of the same BNNT with reduced lengths as a result of three consecutive cuttings at three different locations. The left image shows the original BNNT before cutting. (d) AFM image of one fractured BNNT with the resulting two tube segments staying largely intact. The inset image shows a zoomed-in view of the broken site. The scale bars in (b), (c) and (d) represent 500, 100 and 500 nm, respectively.

can be calculated provided that its normal and torsional spring constants are known.

The event of cutting a nanotube using an AFM probe can be identified from the recorded AFM line profile, and the morphology of the fractured nanotube can be measured by using AFM imaging techniques. Under relatively small collision forces, the AFM tip may just slide across the nanotube surface, which results in the nanotube being merely deformed, instead of being cut, and the measured AFM line scanning profile records the cross-sectional topography of the deformed nanotube. When the nanotube is cut by the AFM tip, a nearly zero tube height is expected in the recorded AFM line scanning height profile.

We employed high quality BNNTs produced using a pressurized vapor/condenser (PVC) method [52] in this study. Our recent studies have revealed that PVC-synthesized BNNTs mostly have 1–4 tube walls and that double-walled tubes of about 2–4 nm in outer diameter have a dominant presence [31]. The scanning electron microscopy (SEM) image in figure 1(b) shows several extruding as-synthesized BNNTs and the inset high resolution transmission electron

microscopy (HRTEM) image shows a representative double-walled BNNT (DW-BNNT) of 2.9 nm in outer diameter.

Two types of nanotube fracture modes were observed in our AFM-based nanotube cutting measurements: (1) the shortening of nanotube length; (2) the formation of fracture slits. The first nanotube cutting mode is represented by the AFM images presented in figure 1(c) showing the results of three consecutive cuttings of one nanotube using the same AFM probe. The original tube, shown in the left image in figure 1(c), possesses an outer diameter of 2.8 nm and a length of 540 nm. The tube length was reduced to 370, 340 and 240 nm respectively after three consecutive cuttings at various locations. Therefore, small tube segments of 170, 30 and 100 nm in length were removed consecutively and respectively from the tube. It is noticed from these AFM images that the remaining tube segment following each cutting stayed at its original location on the substrate, indicating that its adhesion force with the substrate was strong enough to keep it from any motion on the substrate during the tip–tube collision and the nanotube fracture events. The removed tube segments, each of which had a smaller

length compared to the remaining one, disappeared from the recorded AFM images. This is most probably due to their substantial motion on the substrate caused by the collision force. For some cutting measurements, our AFM imaging results showed that the removed tube segments remained close-by, but had a clear separation from the other intact tube segment(s). The second nanotube fracture mode is represented by the AFM image shown in figure 1(d). The tested tube had an original length of 2.1 μm (straight segment only) and was cut by an AFM tip around the central length position. The resulting two tube segments remained largely at a standstill at the tube's original position with noticeable deformations only around the tube's broken site. It is noticed from the inset AFM image that there is a visible slit between the two seemingly still connected tube segments. Our observation of these two types of nanotube fracture modes shows that (i) it is feasible to control the tube length and the cutting position by using our AFM nanomechanical cutting scheme and (ii) the morphology of the resulting fractured nanotube segments is influenced by the cutting position, their lengths and their adhesion interaction with the substrate. We want to point out that the atomic processes behind these two cutting modes are both based on fracture of the tube and thus are fundamentally the same. Our measurements show that the event of cutting nanotubes by using AFM probes depends on several factors, including the normal compressive load applied to the AFM probe, the scribing velocity, the frictional interaction at the tip–tube collision contact interface, the structural configuration and transverse deformability of the nanotubes, etc. In the following sections, we present quantitative data and analysis of the nanotube cutting measurements and provide insights into the roles of the above-mentioned factors in the nanotube cutting process.

2.2. Quantitative nanomechanical cutting of BNNTs

The AFM images presented in figure 2(a) show one BNNT after being cut consecutively at two different positions by using the AFM cutting scheme illustrated in figure 1(a). The original cross-sectional height of the tested tube (h_0) is measured to be of 3.21 nm from its topography image (left image in figure 2(a)). The outer diameter of the tube (D_{nt}) is estimated to be about 2.87 nm by considering $D_{nt} = h_0 - t$ [53], in which $t = 0.34$ nm is the inter-layer distance of the B–N sheet [52]. The fragmentation of the tube can be categorized as the first nanotube fracture mode that is discussed in section 2.1. For both cutting events, the scribing velocity of the AFM tip was set at 240 nm s^{-1}. The compressive load applied to the AFM probe (P) was set to start from 0.05 nN and increase at an interval of 1–2 nN until the nanotube was cut by the AFM tip. Figure 2(b) shows several selected AFM topography and lateral force profiles recorded during the first cutting measurement. The cross-section height of the tube gradually decreased with increase of the normal compressive load P up to 7 nN, and then collapsed and became nearly zero for $P = 9$ nN, indicating the occurrence of nanotube fracture. Therefore, the required compressive load to fracture the nanotube must be a

value within the range of 7–9 nN and is denoted as 8 ± 1 nN in this paper. The corresponding lateral force signals showing the torsional deflections of the AFM cantilever are also presented in figure 2(b). When the AFM tip just slides on the substrate surface, the torsional deflection of the AFM cantilever is caused by the frictional force between the AFM tip and the substrate. After the AFM tip collides with the nanotube surface, the resulting lateral collision force increases the torsional deflection of the AFM cantilever and causes a spike in the recorded lateral force signal. It should be emphasized that the measured lateral collision force is ascribed to both the tip/tube collision deformations and their topographic effects [54, 55]. The recorded lateral force profiles show that, prior to the nanotube cutting event (i.e. $P \le 7$ nN), both the frictional force between the AFM tip and the substrate and the peak lateral force due to the tip–tube collision increase with the applied compressive load P. There was no clearly visible peak in the recorded lateral force profile when the nanotube was cut by the AFM tip.

It is also noticed from figure 2(b) that the peak lateral force occurred when the AFM tip was lifted from the substrate and collided with the nanotube in a sliding-up configuration, as illustrated by the inset free-body diagram. In such a tip–tube collision contact configuration, the compressive load applied to the AFM probe is supported purely by the nanotube [34]. Therefore, the stress developed in the tube depends not only on the compressive load P and the peak lateral force F_L, but also on the contact angle θ between these two forces on the tip–tube collision contact (see the inset free-body diagram in the top panel of figure 2(b)). The contact angle θ is calculated as the slope angle of the height profile at the position corresponding to the peak lateral force. The respective dependences of the measured peak lateral force, the nanotube cross-section height and the contact angle θ on the normal compressive load P during the first cutting measurement are shown in the plots presented in figure 2(c), which are also contrasted with the respective data from the second cutting measurement. Our results show that the peak lateral force applied to the AFM tip increased linearly with the applied compressive load, while the contact angle of the AFM tip and the tube ($\sim 20°$) seems largely independent of the compressive load for the employed scribing velocity. The peak lateral force corresponding to the required normal cutting force (i.e. 8 nN) is obtained through linear extrapolation, as shown in the top panel in figure 2(c), and is calculated as 8.2 ± 0.2 nN and represented by an empty circle in the plot. The corresponding contact angle is estimated as the average value of all the measured contact angles.

The second cutting measurement that was performed on the same tube essentially repeated the first measurement at a different position by following the same procedure. The nanotube was cut under the same compressive load P and the lateral peak force found in the first cutting measurement. It can be seen from figure 2(c) that the results of these two cutting measurements on the same tube are in good agreement and demonstrate the consistency and reproducibility of our nanotube cutting measurements.

The number of tube walls in the tested BNNT is an important structural parameter to interpret the nanotube
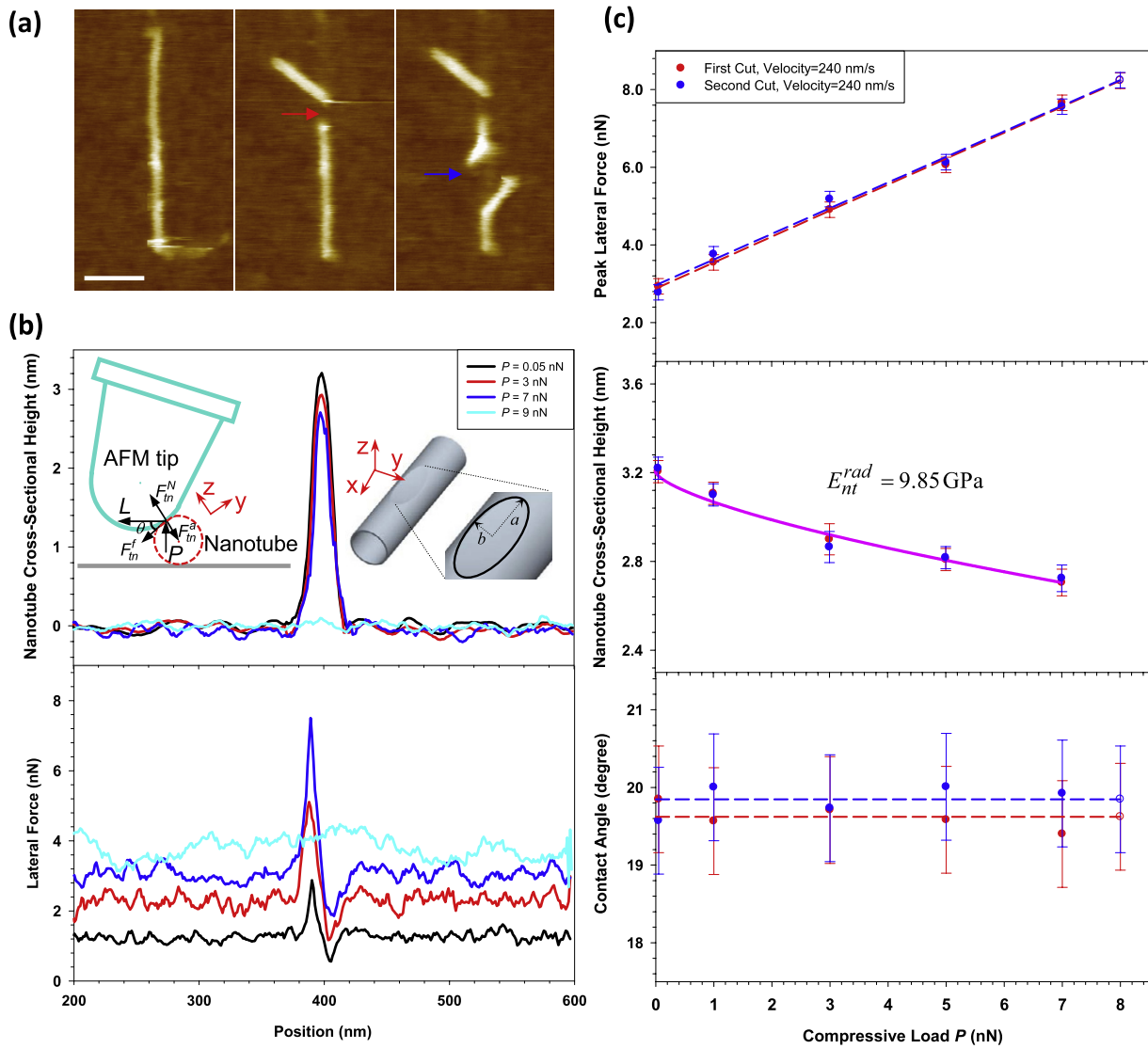
(a)

(b)

(c)

Figure 2. (a) Selected AFM images showing one BNNT cutting measurement. The original straight tube as shown in the left image was cut consecutively by an AFM tip at two different positions indicated by the red and blue arrows, respectively. For both cutting tests, the scribing velocity of the AFM tip was set at 240 nm s^{-1}. The scale bar represents 100 nm. (b) Selected AFM line scanning height (top) and lateral force (bottom) profiles recorded on the BNNT shown in (a) under four selected compressive loads during the first cutting test. The left inset in the top panel shows a free-body diagram of an AFM tip colliding with a nanotube in a sliding-up position. The right inset illustrates the tip–tube collision contact elliptical interface. (c) The respective dependences of the measured peak lateral force (top), the nanotube cross-section height (middle) and the calculated contact angle on the tip–tube collision interface (bottom) on the compressive load applied to the AFM tip for both cutting measurements shown in (a). The dotted lines in the top panel are the linear fitting curves, while the dotted lines in the bottom panel indicate the average values of the measured contact angles. The solid line in the middle plot represents theoretical fitting curve using equation (4).

cutting measurement. Because the nanotube remains on a solid substrate and cannot be inspected directly using HRTEM techniques, we identified the wall number of the tube based on its outer diameter measured by AFM and its radial rigidity. Our recent studies show that the effective radial modulus (E_{nt}^{rad}) can be considered as a signature of the radial rigidity of a BNNT, which correlates well with the tube's wall number and outer diameter [31]. For instance, for DW-BNNTs, their effective radial moduli can be reasonably approximated as a simple power function of the tube diameter, given by $E_{nt}^{rad} = 241.3D_{nt}^{-3.295}$, in which E_{nt}^{rad} and D_{nt} are in units of GPa and nm, respectively [31]. The outer diameter of the tested

tube shown in figure 2(a) (2.87 nm) indicates that it can be either a single- or double-walled tube [31]. We evaluate the radial rigidity of the tube by calculating its effective radial modulus using a Hertzian contact mechanics model given in equation (4) (see section 4) [30, 31]. By fitting the measured cross-section height versus the applied compressive load profile (the plot shown in the middle panel of figure 2(c)), the effective radial modulus of the tested tube is calculated to be 9.85 GPa, which is consistent with the reported data for DW-BNNTs [31].

As discussed earlier, the AFM-based nanotube cutting event is essentially a collision/impact phenomenon. There-

fore, the scribing velocity of the AFM tip is expected to have a prominent influence on the nanotube cutting measurement. We performed a comparison study of cutting the same nanotubes using different scribing velocities. One representative study was performed on a BNNT of 3.0 nm in original outer diameter with two selected scribing velocities of 240 and 1200 nm s^{-1}, respectively. Our measurements show that the tube was cut under a compressive load of 8 ± 1 nN and a corresponding peak lateral force of 8.6 ± 0.2 nN for a scribing velocity of 240 nm s^{-1}, while the tube was cut again at a different position under a compressive load of 12 ± 1 nN and a peak lateral force of 12.3 ± 0.2 nN for a velocity of 1200 nm s^{-1}. Our results clearly show that the required compressive load leading to the cutting of the nanotube increases by about 50% as a result of the increased scribing velocity. The plots presented in figure 3 show the respective dependences of the measured peak lateral force, the nanotube cross-section height and the contact angle on the compressive load for these two cutting measurements. Our analysis shows that the tested tube was a double-walled nanotube based on its outer diameter and effective radial modulus. The results presented in figure 3 (top panel) show that the peak lateral force increases with the impact velocity. The recorded peak lateral forces corresponding to the tube cutting show a similar percentage increase to that of the required normal cutting load due to the increase of the impact velocity. The observed influence of the impact velocity on the required normal and lateral cutting forces can be qualitatively explained using dynamic fracture mechanics theory [56]. The impact-induced fracture of a nanotube can be ascribed to the initiation and growth of cracks in the nanotube. The dynamic loading results in a higher stress-intensity factor compared with static loading. By assuming that the failure time equals the failure incubation time (a characteristic relaxation time upon micro-fracture of a material), the dynamic fracture strength of a material is estimated to be double its static strength [56]. For the comparison of two impact velocities such as those employed in this study, the fracture strength is expected to increase by less than one fold, which is consistent with our observation of a 50% increase of the required cutting force.

We performed the nanotube cutting measurements on a number of different BNNTs. Among them, 18 tubes, including the two tested tubes shown in figures 2 and 3, were identified to be DW-BNNTs with their outer diameters ranging from 2.26 to 4.28 nm. Figures 4(a) and (b) show the measured compressive and lateral forces respectively leading to the cutting of these DW-BNNTs. The solid blue dots represent cutting experiments performed at a scribing velocity of 1200 nm s^{-1}, while the red dots correspond to measurements performed at 240 nm s^{-1}. The empty blue and red squares represent the data corresponding to the two cutting experiments shown in figure 3, respectively. The red empty triangle represents the data for the measurements shown in figure 2. Our results show that the required compressive and lateral forces are rather comparable and are within the range of 5–23 nN and 8–17 nN, respectively. Figure 4(a) shows a generally decreasing trend of the required compressive load to cut a nanotube with respect to its outer diameter. In addition,
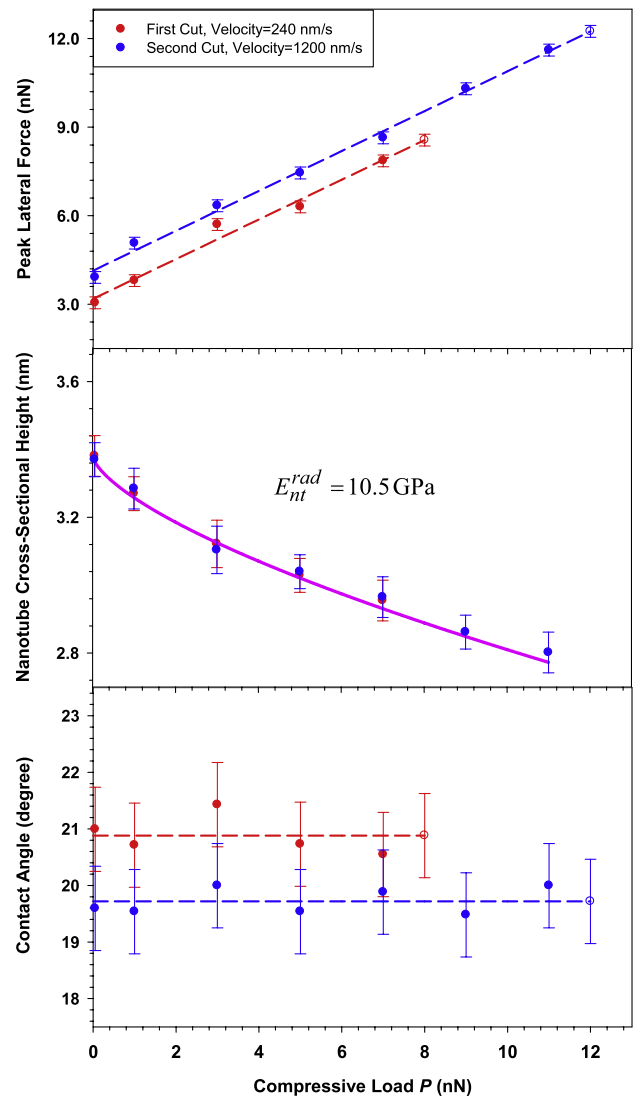

Figure 3. Measurements on one BNNT that was cut at two different positions with the AFM scribing velocity set at 240 nm s^{-1} for the first cut and 1200 nm s^{-1} for the second cut, respectively. The measured nanotube cross-sectional height data (dots) in the middle plot are theoretically fitted by the solid line based on the Hertzian contact model given by equation (4).

a higher compressive load is needed when cutting the tube at a higher impact velocity. No obvious trend is displayed in figure 4(b) on the dependence of the lateral force on the nanotube's outer diameter. However, our data reveal that a higher lateral force is needed when cutting the tube at a higher impact velocity.

From an energy point of view, the nanotube cutting process can be considered as a result of the balance between the fracture energy and the external work performed by the cutting force. Considering a greatly simplified scenario where a DW-BNNT is cut by a pure lateral collision force F_L by disrupting the nanotube lattices at both the inner and the outer tube shells, the fracture energy is given by $\pi \cdot \gamma \cdot t \cdot [D_{nt} + (D_{nt} - 2t)]$, in which $\gamma = 8$ N m^{-1} is the fracture energy per unit area of BNNT [57]. The external work can be expressed as $\bar{F}_L \cdot D_{nt}$, in which $\bar{F}_L$ represents the required
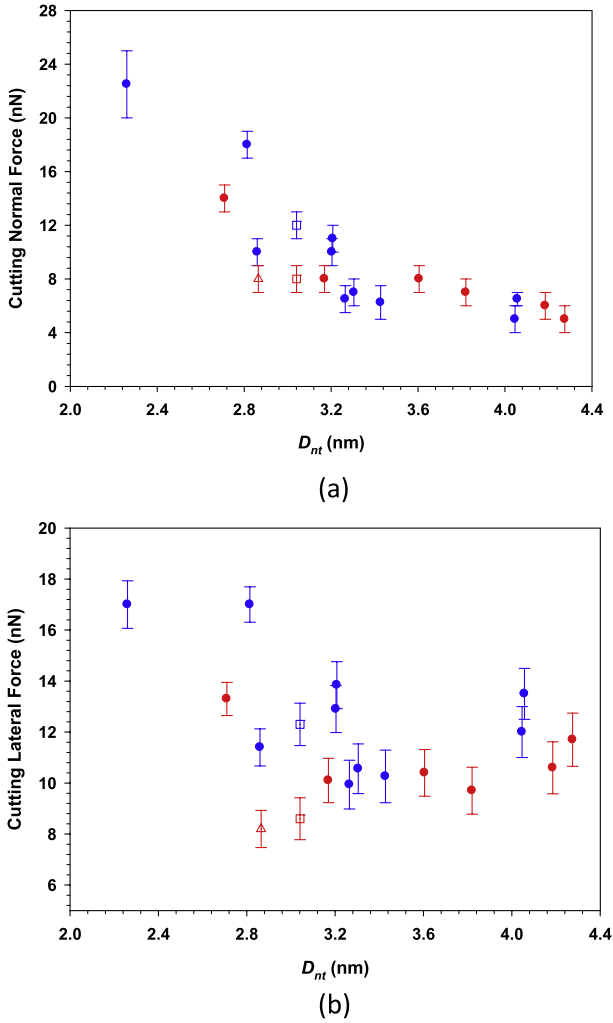
Figure 4. The measured (a) normal compressive and
(b) corresponding lateral cutting force based on 19 different
DW-BNNT cutting measurements. The blue dots represent data
recorded for cutting measurements performed at a scribing velocity
of 1200 nm s^{-1}, while the red dots are for measurements performed
at a velocity of 240 nm s^{-1}. The red empty triangle represents the
data for the measurement shown in figure 2. The blue and red empty
squares represent the data corresponding to the two cutting
experiments shown in figure 3.

average lateral cutting force. From the energy balance, we
obtain $\bar{F}_L = 2\pi\gamma t(1 - \frac{t}{D_{nt}})$. For the DW-BNNTs tested in
this work, $\bar{F}_L$ is estimated to be within 14.5–15.7 nN, which
is quite consistent with the cutting forces recorded in our
measurements.

2.3. Fracture strength of BNNTs

To reveal the nature of the fracture strength and the
microscopic mechanism of cutting nanotubes using AFM,
we interpret our nanomechanical cutting measurements using
Hertzian contact mechanics models. In this model, we
simplify the tip–tube collision as an elastic contact between
a sphere and a cylinder and assume that the nanotube fracture
is caused by the stress in the tube due to the combined normal
compressive load and tangential frictional force exerted by the
AFM tip during the tip–tube collision process. The free-body

diagram shown in figure 2(b) depicts the forces acting on
the cantilever tip, including the interaction forces at the
tip–tube collision contact. If we assume that the AFM tip
and the nanotube stay in an equilibrium at the moment of
the peak collision force, the normal and frictional forces at
the tip–tube collision contact are given as $F_{tn}^N = P\cos\theta +
F_L\sin\theta + F_{tn}^a$ and $F_{tn}^f = P\sin\theta - F_L\cos\theta$, respectively, in
which F_{tn}^a is the adhesion force at the tip–tube contact, and
was measured to be about 3–4 nN by operating the AFM
in the force modulation mode [55]. It is well known that
the interface of an elastic cylinder–sphere contact exhibits
an elliptical shape, as illustrated in the deformed nanotube
configuration shown in the right inset drawing in the top
panel of figure 2(b). The projected elliptical contact region
on the x–y plane, Ω, is given by $(x^2/a^2) + (y^2/b^2) \le 1$ for
$z = 0$, in which a is the semi-major axis in the x direction
and b is the semi-minor axis in the y direction [58]. By
using the theory of contact mechanics [59] and considering
a Hertzian pressure distribution, the semi-minor axis b of the
elliptic-shape region can be determined from the following
Hertzian expression [58]:

$$b = \left\{ \frac{3kE(e)}{2\pi} F_{tn}^N \left[\frac{D_{nt}R_{tip}}{D_{nt} + R_{tip}} \left(\frac{1 - \nu_{nt}^2}{E_{nt}} + \frac{1 - \nu_{tip}^2}{E_{tip}} \right) \right] \right\}^{1/3}$$
(1)

where R_{tip} is the radius of the AFM tip; E and ν represent
the elastic modulus and Poisson's ratio, respectively, for the
material of the BNNT (subscript-nt) and the AFM tip (tip).
The values $\nu_{tip} = 0.16$, $\nu_{nt} = 0.2$ and $E_{tip} = 74$ GPa [31] are
employed in the present Hertzian contact model. Because the
majority of the BNNT deformation occurs along its radial
direction, its elastic modulus E_{nt} in equation (1) can be
reasonably approximated by its effective radial modulus E_{nt}^{rad}
if the tube is assumed as an elastic body. $k = b/a$ is the ratio
of the semi-minor and semi-major axes of the elliptic-shape
contact and can be determined from the following expression:

$$1 + \frac{R_{tip}}{R_{nt}} = \frac{(1/k^2)E(e) - K(e)}{K(e) - E(e)},$$
(2)

where $e = \sqrt{1 - k^2}$, and $K(e) = \int_0^{\pi/2}(1 - e^2\sin\theta^2)^{-1/2}d\theta$
and $E(e) = \int_0^{\pi/2}(1 - e^2\sin\theta^2)^{1/2}d\theta$ are complete elliptic
integrals of the first and second kinds, respectively.

The resulting total stress tensor σ on the contact region
Ω can be obtained by superimposing the two stress tensors
caused by the normal compressive load F_{tn}^N and the tangential
frictional force F_{tn}^f, respectively. These two stress tensors are
denoted as σ^N and σ^f, respectively, and are given as [59, 60]

$$\sigma^N = \begin{bmatrix} \sigma_{xx}^N & \sigma_{xy}^N & 0 \\ \sigma_{xy}^N & \sigma_{yy}^N & 0 \\ 0 & 0 & \sigma_{zz}^N \end{bmatrix} \quad \text{and}$$

$$\sigma^f = \begin{bmatrix} \sigma_{xx}^f & \sigma_{xy}^f & 0 \\ \sigma_{xy}^f & \sigma_{yy}^f & \sigma_{yz}^f \\ 0 & \sigma_{yz}^f & 0 \end{bmatrix}.$$
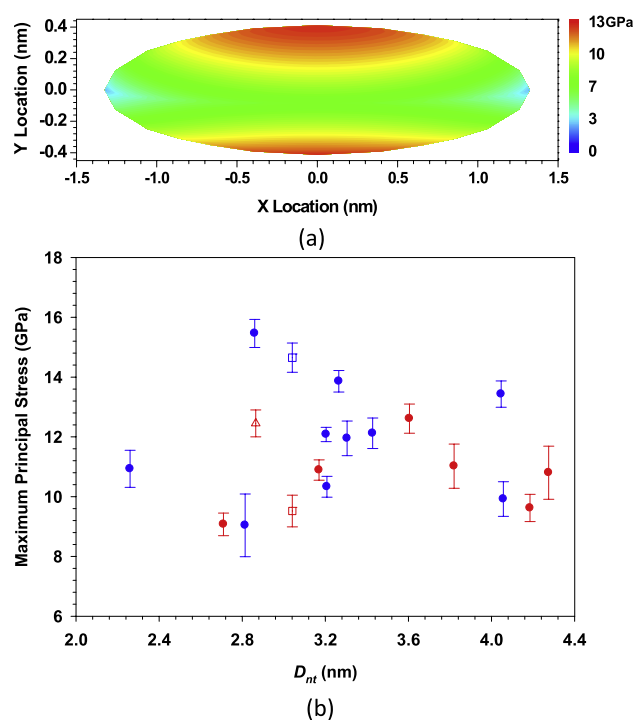(3)

Figure 5. (a) The contour plot of the calculated maximum principal stress (magnitude) at the AFM tip–nanotube collision interface for the first cutting measurement shown in figure 2; (b) the calculated fracture strengths of the BNNTs employed in the cutting measurements based on the maximum principal stress criterion.

Previous studies have reported brittle behavior in the fracture of nanotube structures at room temperature [37, 61–64]. Here we evaluate the failure of BNNTs using the maximum principal stress or Rankine criterion. Figure 5(a) shows the contour plot of the calculated maximum principal stress (magnitude) at the tip–tube elliptical contact interface for the first nanotube cutting measurement shown in figure 2(a). The major and minor axes of the elliptical contact region are calculated to be $a = 1.324$ nm and $b = 0.412$ nm, respectively. Our results show that the maximum principal stress is found to be a tensile stress of 12.45 GPa at $x = 0$ and $y = -b$, indicating that the fracture of the nanotube was initiated at the lower end point along the minor axis on the elliptical contact interface. The calculated maximum principal stress is taken as the fracture strength of the nanotube. Figure 5(b) shows the calculated fracture strengths of the tested DW-BNNTs based on the Rankine criterion, which are found to be within the range of 9.1–15.5 GPa. Our data on the fracture strength of BNNTs are consistent with the values reported by Tang *et al* [64] (8 GPa) and by Wei *et al* [37] (8.5–33.2 GPa), both of which were obtained by *in situ* TEM tensile testing techniques. The reasonably good agreement on the mechanical strength of BNNTs suggests that our proposed AFM-based nanomechanical cutting technique is promising as a new mechanical testing technique for characterizing the mechanical strength of tubular nanostructures.

We want to point out that BNNTs undergo complex deformation processes during their collision with AFM tips, which involve bending, stretching and rotation of the B–N bonds in the nanotube. The contact mechanics model employed in this work is a simplified theoretical model and helps to facilitate the interpretation of our experimental measurements. This model takes into account the major material properties and overall deformations and stresses in the tube during the tip–tube collision process, while neglecting many other features, such as the anisotropic properties of BNNTs and the effect of the tube/substrate adhesion on the tube cross-section deformation. For instance, BNNTs are known to have much higher elastic moduli along their axial directions than their radial directions [65], while the contact mechanics model given by equation (1) was derived based on contact between isotropic elastic bodies. The calculated fracture strength of BNNTs is somewhat underestimated by using the effective radial moduli of BNNTs in this contact mechanics model. This is because the lower modulus employed results in a larger contact region at the tip–tube collision interface, which leads to lower contact stresses. Therefore, it is essential to have a more comprehensive theoretical model in order to achieve a more precise characterization of the mechanical properties of nanotubes from the AFM cutting measurements. On the other hand, it would be an intractable, if not impossible, task to devise an analytical model that takes into account all these delicate features. Therefore, new theoretical models based on advanced computational approaches, such as finite element methods (FEMs) and atomistic simulation techniques, are warranted to further investigate the deformation/fracture of BNNTs [66–68] in AFM-based cutting experiments to provide more accurate insights into the structural and mechanical properties of BNNTs.

3. Conclusions

In this paper, we present a quantitative nanomechanical study of the cutting of individual BNNTs using AFM-based scribing techniques. The nanomechanical cutting measurements characterized the mechanical response of the nanotube during the tip–tube collision process and quantified the required normal compressive load and the corresponding lateral peak collision force that led to the nanotube fracture. The fracture strengths of the tested DW-BNNTs were characterized using contact mechanics theory and found to be within the range 9.1–15.5 GPa, which is consistent with the reported tensile testing data in the literature. The results from this nanomechanical study clearly demonstrate that the AFM-based nano-scribing technique can not only be used to precisely control the lengths of individual nanotubes, but is also promising as a new nanomechanical testing technique for characterizing the mechanical properties of tubular nanostructures. The precise length control of nanotubes using nanomechanical cutting techniques is useful for the optimal design and manufacture of nanotube-based material systems and devices.

4. Experiments and methods

4.1. BNNT sample preparation

The BNNTs employed were synthesized using a pressurized vapor/condenser (PVC) method [52]. The as-synthesized

BNNTs were separated in deionized (DI) water by ultrasonication for two hours with the aid of sodium dodecylbenzenesulfonate (NaDDBS) purchased from Sigma-Aldrich, Co. [30, 31]. Small drops of dispersed BNNT solution were first deposited on clean Si wafers by spin-coating or copper grids with lacey support films (Ted Pella, Inc.) and then repeatedly washed using DI water to remove residue surfactants. Subsequently, BNNT samples were air-dried for AFM and TEM measurements.

4.2. SEM and TEM characterization

The SEM characterization of the BNNTs was performed using a Zeiss Supra 55 field emission SEM. The high resolution transmission electron microscopy (HRTEM) characterization of the BNNTs was performed using a JEM 2100F TEM (JEOL Ltd) operated at accelerating voltages of 120–200 kV.

4.3. AFM characterization

The AFM imaging and nanomechanical measurements were performed using a Park Systems XE-70 AFM that was housed inside an environmental chamber. The employed AFM was incorporated with a closed-loop feedback control feature in the *XYZ* axes, and operated in contact mode at room temperature with the humidity set at 10%. Rectangular silicon AFM cantilevers (model CSG 10, NT-MDT) with a nominal length of 225 μm, width of 30 μm and thickness of 1 μm were employed in the AFM measurements. The employed CSG 10 AFM probes have nominal spring constants of 0.11 N m^{-1} and their actual spring constants were calibrated using the thermal tuning method [69] and were found to be in the range of 0.09–0.25 N m^{-1}. The thermal-induced rms normal deflection noise of the employed AFM probes at the tip position at 1–500 Hz bandwidth was measured to be 0.71 Å, and the corresponding rms force noise was calculated to be about 6–18 pN. The lateral force applied to the AFM tip was calculated as $L = U \cdot \alpha$, in which U is the measured voltage signal in response to the horizontal motion of the reflected laser spot on the photo-detector; α is known as the lateral sensitivity of the cantilever, a quantity correlating the lateral force applied to the AFM tip with the horizontal motion of the laser spot on the photo-detector. We calibrated each AFM cantilever by following a two-slope wedge method using a TGG01 silicon grating [70] and their lateral sensitivities were found to be within the range of 0.039–0.11 nN mV. The thermal-induced rms lateral force noise was measured to be about 0.27 mV, corresponding to an rms lateral force noise of about 11–30 pN. The tip radii of our employed AFM probes were estimated to be 7–20 nm based on the recorded nanotube AFM images [69].

4.4. The Hertzian contact mechanics model to determine the radial rigidity of the BNNTs

The measured BNNT cross-section height h when the AFM tip slides right on top of a nanotube cross-section on a flat Si

substrate under a compressive load P is given as [71]

$$h = 2h_0 - \left(\frac{P}{k_1\sqrt{h_0}}\right)^{2/3} - \left(\frac{P}{k_2\sqrt{\left[1/h_0 + 1/R_{\mathrm{tip}}\right]^{-1}}}\right)^{2/3}$$
$$+ \left(\frac{P}{k_3\sqrt{R_{\mathrm{tip}}}}\right)^{2/3}, \tag{4}$$

in which $k_1 = \frac{4}{3}\left(\frac{1-\nu_{\mathrm{nt}}^2}{E_{\mathrm{nt}}^{\mathrm{rad}}} + \frac{1-\nu_{\mathrm{sub}}^2}{E_{\mathrm{sub}}}\right)^{-1}$, $k_2 = \frac{4}{3}\left(\frac{1-\nu_{\mathrm{tip}}^2}{E_{\mathrm{tip}}}\right)^{-1}$ and $k_3 = \frac{4}{3}\left(\frac{1-\nu_{\mathrm{tip}}^2}{E_{\mathrm{tip}}} + \frac{1-\nu_{\mathrm{sub}}^2}{E_{\mathrm{sub}}}\right)^{-1}$. The effective radial modulus of the BNNTs, $E_{\mathrm{nt}}^{\mathrm{rad}}$, can be obtained by fitting the measured curve of the compressive load P versus the nanotube cross-section height h by using equation (4). More details about the characterization of the effective radial modulus of the BNNTs can be found in our recent work [30, 31].

Appendix. Stress tensors in cylindrical bodies

A.1. Under normal compressive loads

The stress components in the stress tensor σ^{N} in equation (3) are given as [59, 72]

$$\sigma_{xx}^{\mathrm{N}} = p_0 \left[-2\nu_{\mathrm{nt}}\lambda - (1-2\nu_{\mathrm{nt}})\frac{b}{ae^2}\left\{\left(1 - \frac{b\lambda}{a}\right) - \frac{x}{ae}\right.\right.$$
$$\left.\left.\times \tanh^{-1}\left(\frac{ex}{a+b\lambda}\right) - \frac{y}{ae}\tan^{-1}\left(\frac{aey}{b(b+a\lambda)}\right)\right\}\right], \tag{A.1}$$

$$\sigma_{yy}^{\mathrm{N}} = p_0 \left[-2\nu_{\mathrm{nt}}\lambda - (1-2\nu_{\mathrm{nt}})\frac{b}{ae^2}\left\{\left(\frac{a\lambda}{b} - 1\right) + \frac{x}{ae}\right.\right.$$
$$\left.\left.\times \tanh^{-1}\left(\frac{ex}{a+b\lambda}\right) + \frac{y}{ae}\tan^{-1}\left(\frac{aey}{b(b+a\lambda)}\right)\right\}\right], \tag{A.2}$$

$$\sigma_{xy}^{\mathrm{N}} = p_0 \left[-(1-2\nu_{\mathrm{nt}})\frac{b}{ae^2}\left\{\frac{y}{ae}\tanh^{-1}\left(\frac{ex}{a+b\lambda}\right)\right.\right.$$
$$\left.\left. - \frac{x}{ae}\tan^{-1}\left(\frac{aey}{b(b+a\lambda)}\right)\right\}\right], \tag{A.3}$$

$$\sigma_{zz}^{N} = p_0 \left(1 - \frac{x^2}{a^2} - \frac{y^2}{b^2}\right)^{1/2}, \tag{A.4}$$

where $p_0 = \frac{3F_{tn}^{N}}{2\pi ab}$ and $\lambda = \sqrt{1 - (x/a)^2 - (y/b)^2}$.

A.2. Under tangential frictional loads

The stress components in the stress tensor σ^f in equation (3) are given as [60, 73]

$$\sigma_{xx}^{f} = \frac{q_0 y}{b(1 - \nu_{nt})}(kI_2 - 2\nu_{nt}I_1), \tag{A.5}$$

$$\sigma_{yy}^{f} = \frac{q_0 y}{b(1 - \nu_{nt})}(2I_1 - k\nu_{nt}I_2), \tag{A.6}$$

$$\sigma_{xy}^{f} = \frac{q_0 x}{a}\left(kI_3 - \frac{1}{2}I_2\right), \tag{A.7}$$

$$\sigma_{yz}^{f} = q_0 \left(1 - \frac{x^2}{a^2} - \frac{y^2}{b^2}\right)^{1/2}, \tag{A.8}$$

where $q_0 = \frac{3F_{tn}^{f}}{2\pi ab}$, $I_1 = \frac{E(e) - k^2 K(e)}{e^2} - \nu_{nt}\frac{(2-e^2)E(e) - 2k^2 K(e)}{e^4}$, $I_2 = 2k\nu_{nt}\frac{(1+k^2)K(e) - 2E(e)}{e^4}$ and $I_3 = \frac{K(e) - E(e)}{e^2} + \nu_{nt}\frac{2E(e) - (1+k^2)K(e)}{e^4}$.

References

[1] Xu H, Abe H, Naito M, Fukumori Y, Ichikawa H, Endoh S and Hata K 2010 Efficient dispersing and shortening of super-growth carbon nanotubes by ultrasonic treatment with ceramic balls and surfactants *Adv. Powder Technol.* **21** 551–5

[2] Geohegan D B, Puretzky A A, Ivanov I N, Jesse S, Eres G and Howe J Y 2003 *In situ* growth rate measurements and length control during chemical vapor deposition of vertically aligned multiwall carbon nanotubes *Appl. Phys. Lett.* **83** 1851–3

[3] Cheng C, Bukkapatnam S T S, Raff L M and Komanduri R 2012 Towards control of carbon nanotube synthesis process using prediction-based fast Monte Carlo simulations *J. Manuf. Syst.* **31** 438–43

[4] Han J-H, Graff R A, Welch B, Marsh C P, Franks R and Strano M S 2008 A mechanochemical model of growth termination in vertical carbon nanotube forests *ACS Nano* **2** 53–60

[5] Pierard N, Fonseca A, Colomer J F, Bossuot C, Benoit J M, Van Tendeloo G, Pirard J P and Nagy J B 2004 Ball milling effect on the structure of single-wall carbon nanotubes *Carbon* **42** 1691–7

[6] Chen J, Dyer M J and Yu M F 2001 Cyclodextrin-mediated soft cutting of single-walled carbon nanotubes *J. Am. Chem. Soc.* **123** 6201–2

[7] Rubio N, Fabbro C, Herrero M A, de la Hoz A, Meneghetti M, Fierro J L G, Prato M and Vázquez E 2011 Ball-milling modification of single-walled carbon nanotubes: purification, cutting, and functionalization *Small* **7** 665–74

[8] Wang S, Liang Z, Wang B, Zhang C and Rahman Z 2007 Precise cutting of single-walled carbon nanotubes *Nanotechnology* **18** 055301

[9] Vichchulada P, Cauble M A, Abdi E A, Obi E I, Zhang Q and Lay M D 2010 Sonication power for length control of single-walled carbon nanotubes in aqueous suspensions used for 2-dimensional network formation *J. Phys. Chem.* C **114** 12490–5

[10] Shelimov K B, Esenaliev R O, Rinzler A G, Huffman C B and Smalley R E 1998 Purification of single-wall carbon nanotubes by ultrasonically assisted filtration *Chem. Phys. Lett.* **282** 429–34

[11] Yanagi H, Sawada E, Manivannan A and Nagahara L A 2001 Self-orientationof short single-walled carbon nanotubes deposited on graphite *Appl. Phys. Lett.* **78** 1355–7

[12] Hennrich F, Krupke R, Arnold K, Rojas Stütz J A, Lebedkin S, Koch T, Schimmel T and Kappes M M 2007 The mechanism of cavitation-induced scission of single-walled carbon nanotubes *J. Phys. Chem.* B **111** 1932–7

[13] Tsang S C, Chen Y K, Harris P J F and Green M L H 1994 A simple chemical method of opening and filling carbon nanotubes *Nature* **372** 159–62

[14] Ziegler K J, Gu Z, Shaver J, Chen Z, Flor E L, Schmidt D J, Chan C, Hauge R H and Smalley R E 2005 Cutting single-walled carbon nanotubes *Nanotechnology* **16** S539

[15] Chen Z, Kobashi K, Rauwald U, Booker R, Fan H, Hwang W-F and Tour J M 2006 Soluble ultra-short single-walled carbon nanotubes *J. Am. Chem. Soc.* **128** 10568–71

[16] Liu J *et al* 1998 Fullerene pipes *Science* **280** 1253–6

[17] Ziegler K J, Gu Z, Peng H, Flor E L, Hauge R H and Smalley R E 2005 Controlled oxidative cutting of single-walled carbon nanotubes *J. Am. Chem. Soc.* **127** 1541–7

[18] Lustig S R *et al* 2003 Lithographically cut single-walled carbon nanotubes: controlling length distribution and introducing end-group functionality *Nano Lett.* **3** 1007–12

[19] Gu Z, Peng H, Hauge R H, Smalley R E and Margrave J L 2002 Cutting single-wall carbon nanotubes through fluorination *Nano Lett.* **2** 1009–13

[20] Wei X, Chen Q, Liu Y and Peng L 2007 Cutting and sharpening carbon nanotubes using a carbon nanotube 'nanoknife' *Nanotechnology* **18** 185503

[21] Liu P, Arai F and Fukuda T 2006 Cutting of carbon nanotubes assisted with oxygen gas inside a scanning electron microscope *Appl. Phys. Lett.* **89** 113104

[22] Banhart F, Li J and Terrones M 2005 Cutting single-walled carbon nanotubes with an electron beam: evidence for atom migration inside nanotubes *Small* **1** 953–6

[23] Yuzvinsky T D, Fennimore A M, Mickelson W, Esquivias C and Zettl A 2005 Precision cutting of nanotubes with a low-energy electron beam *Appl. Phys. Lett.* **86** 053109

[24] Venema L C, Wildöer J W G, Tuinstra H L J T, Dekker C, Rinzler A G and Smalley R E 1997 Length control of individual carbon nanotubes by nanostructuring with a scanning tunneling microscope *Appl. Phys. Lett.* **71** 2629–31

[25] Kim D-H, Koo J-Y and Kim J-J 2003 Cutting of multiwalled carbonnanotubes by a negative voltage tip of an atomic force microscope: a possible mechanism *Phys. Rev.* B **68** 113406

[26] Postma H W C, Sellmeijer A and Dekker C 2000 Manipulation and imaging of individual single-walled carbon nanotubes with an atomic force microscope *Adv. Mater.* **12** 1299–302

[27] Tombler T W, Zhou C W, Alexseyev L, Kong J, Dai H J, Lei L, Jayanthi C S, Tang M J and Wu S Y 2000 Reversible electromechanical characteristics of carbon nanotubes under local-probe manipulation *Nature* **405** 769–72

[28] Falvo M R, Taylor R M, Helser A, Chi V, Brooks F P, Washburn S and Superfine R 1999 Nanometre-scale rolling and sliding of carbon nanotubes *Nature* **397** 236–8

[29] Strus M C, Zalamea L, Raman A, Pipes R B, Nguyen C V and Stach E A 2008 Peeling force spectroscopy: exposing the adhesive nanomechanics of one-dimensional nanostructures *Nano Lett.* **8** 544–50

[30] Zheng M, Chen X, Bae I-T, Ke C, Park C, Smith M W and Jordan K 2012 Radial mechanical properties of single-walled boron nitride nanotubes *Small* **8** 116–21

[31] Zheng M, Ke C, Bae I-T, Park C, Smith M W and Jordan K 2012 Radialelasticity of multi-walled boron nitride nanotubes *Nanotechnology* **23** 095703

[32] Zheng M, Zou L-F, Wang H, Park C and Ke C 2012 Engineering radial deformations in single-walled carbon and boron nitride nanotubes using ultrathin nanomembranes *Acs Nano* **6** 1814–22

[33] Zheng M, Zou L, Wang H, Park C and Ke C 2012 Quantifying the transverse deformability of double-walled carbon and boron nitride nanotubes using an ultrathin nanomembrane covering scheme *J. Appl. Phys.* **112** 104318

[34] Chen X, Zheng M, Park C and Ke C 2013 Collision and dynamic frictional properties of boron nitride nanotubes *Appl. Phys. Lett.* **102** 121912

[35] Rubio A, Corkill J L and Cohen M L 1994 Theory of graphitic boron-nitride nanotubes *Phys. Rev.* B **49** 5081–4

[36] Chopra N G, Luyken R J, Cherrey K, Crespi V H, Cohen M L, Louie S G and Zettl A 1995 Boron-nitride nanotubes *Science* **269** 966–7

[37] Wei X L, Wang M S, Bando Y and Golberg D 2010 Tensile tests on individual multi-walled boron nitride nanotubes *Adv. Mater.* **22** 4895–9

[38] Chopra N G and Zettl A 1998 Measurement of the elastic modulus of amulti-wall boron nitride nanotube *Solid State Commun.* **105** 297–300

[39] Arenal R, Wang M S, Xu Z, Loiseau A and Golberg D 2011 Young modulus, mechanical and electrical properties of isolated individual and bundled single-walled boron nitride nanotubes *Nanotechnology* **22** 265704

[40] Hernandez E, Goze C, Bernier P and Rubio A 1998 Elastic properties of C and $B_xC_yN_z$ composite nanotubes *Phys. Rev. Lett.* **80** 4502–5

[41] Ghassemi H M, Lee C H, Yap Y K and Yassar R S 2010 Real-time fracture detection of individual boron nitride nanotubes in severe cyclic deformation processes *J. Appl. Phys.* **108** 024314

[42] Garel J, Leven I, Zhi C, Nagapriya K S, Popovitz-Biro R, Golberg D, Bando Y, Hod O and Joselevich E 2012 Ultrahigh torsional stiffness and strength of boron nitride nanotubes *Nano Lett.* **12** 6347–52

[43] Chang C W, Fennimore A M, Afanasiev A, Okawa D, Ikuno T, Garcia H, Li D Y, Majumdar A and Zettl A 2006 Isotope effect on the thermal conductivity of boron nitride nanotubes *Phys. Rev. Lett.* **97** 085901

[44] Xiao Y, Yan X H, Cao J X, Ding J W, Mao Y L and Xiang J 2004 Specific heat and quantized thermal conductance of single-walled boron nitride nanotubes *Phys. Rev.* B **69** 205415

[45] Lee C H, Xie M, Kayastha V, Wang J S and Yap Y K 2010 Patterned growth of boron nitride nanotubes by catalytic chemical vapor deposition *Chem. Mater.* **22** 1782–7

[46] Ghassemi H M, Lee C H, Yap Y K and Yassar R S 2012 Field emission andstrain engineering of electronic properties in boron nitride nanotubes *Nanotechnology* **23** 105702

[47] Chen Y, Zou J, Campbell S J and Le Caer G 2004 Boron nitride nanotubes: pronounced resistance to oxidation *Appl. Phys. Lett.* **84** 2430–2

[48] Golberg D, Bando Y, Kurashima K and Sato T 2001 Synthesis and characterization of ropes made of BN multiwalled nanotubes *Scr. Mater.* **44** 1561–5

[49] Zhi C Y, Bando Y, Terao T, Tang C C, Kuwahara H and Golberg D 2009 Towards thermoconductive, electrically insulating polymeric composites with boron nitride nanotubes as fillers *Adv. Funct. Mater.* **19** 1857–62

[50] Li Y B, Dorozhkin P S, Bando Y and Golberg D 2005 Controllable modification of SiC nanowires encapsulated in BN nanotubes *Adv. Mater.* **17** 545–9

[51] Chen Z G, Zou J, Liu G, Li F, Cheng H M, Sekiguchi T, Gu M, Yao X D, Wang L Z and Lu G Q 2009 Long wavelength emissions of periodic yard-glass shaped boron nitride nanotubes *Appl. Phys. Lett.* **94** 023105

[52] Smith M W, Jordan K C, Park C, Kim J-W, Lillehei P T, Crooks R and Harrison J S 2009 Very long single- and few-walled boron nitride nanotubes via the pressurized vapor/condenser method *Nanotechnology* **20** 505604

[53] DeBorde T, Joiner J C, Leyden M R and Minot E D 2008 Identifying individual single-walled and double-walled carbon nanotubes by atomic force microscopy *Nano Lett.* **8** 3568–71

[54] Sundararajan S and Bhushan B 2000 Topography-induced contributions to friction forces measured using an atomic force/friction force microscope *J. Appl. Phys.* **88** 4825–31

[55] Lievonen J and Ahlskog M 2009 Lateral force microscopy of multiwalled carbon nanotubes *Ultramicroscopy* **109** 825–9

[56] Pugno N M 2006 Dynamic quantized fracture mechanics *Int. J. Fract.* **140** 159–68

[57] Pugno N, Marino F and Carpinteri A 2006 Towards a periodic table forthe nanomechanical properties of the elements *Int. J. Solids Struct.* **43** 5647–57

[58] Boresi A P and Schmidt R J 2002 *Advanced Mechanics of Materials* (New York: Wiley)

[59] Johnson K L 1987 *Contact Mechanics* (Cambridge: Cambridge University Press)

[60] Sackfield A and Hills D A 1983 Some useful results in the tangentially loaded hertzian contact problem *J. Strain Anal. Eng. Des.* **18** 107–10

[61] Dumitrică T and Yakobson B I 2005 Rate theory of yield in boron nitride nanotubes *Phys. Rev.* B **72** 035418

[62] Zhang P H and Crespi V H 2000 Plastic deformations of boron-nitride nanotubes: an unexpected weakness *Phys. Rev.* B **62** 11050–3

[63] Mielke S L, Belytschko T and Schatz G C 2007 Nanoscale fracture mechanics *Annu. Rev. Phys. Chem.* **58** 185–209

[64] Tang D-M, Ren C-L, Wei X, Wang M-S, Liu C, Bando Y and Golberg D 2011 Mechanical properties of bamboo-like boron nitride nanotubes by *in situ* TEM and MD simulations: strengthening effect of interlocked joint interfaces *ACS Nano* **5** 7362–8

[65] Chiu H-C, Kim S, Klinke C and Riedo E 2012 Morphology dependence of radial elasticity in multiwalled boron nitride nanotubes *Appl. Phys. Lett.* **101** 103109

[66] Feng X, Jiang H, Huang Y, Liu B and Chen J-S 2008 Modeling fracture incarbon nanotubes using a meshless atomic-scale finite-element method *JOM* **60** 50–5

[67] Song J, Jiang H, Wu J, Huang Y and Hwang K-C 2007 Stone–Wales transformation in boron nitride nanotubes *Scr. Mater.* **57** 571–4

[68] Song J, Wu J, Huang Y and Hwang K C 2008 Continuum modeling of boron nitride nanotubes *Nanotechnology* **19** 445705

[69] Gibson C T, Watson G S and Myhra S 1997 Scanning force microscopy—calibrative procedures for 'best practice' *Scanning* **19** 564–81

[70] Ogletree D F, Carpick R W and Salmeron M 1996 Calibration of frictional forces in atomic force microscopy *Rev. Sci. Instrum.* **67** 3298–306

[71] Yang Y H and Li W Z 2011 Radial elasticity of single-walled carbon nanotube measured by atomic force microscopy *Appl. Phys. Lett.* **98** 041901

[72] Sackfield A and Hills D A 1983 Some useful results in the classical Hertz contact problem *J. Strain Anal. Eng. Des.* **18** 101–5

[73] Vermeulen P J and Johnson K L 1964 Contact of nonspherical elastic bodies transmitting tangential forces *J. Appl. Mech.* **31** 338